Indian Journal of Biochemistry & Biophysics
Vol. 62, July 2025, pp. 766-785
DOI: 10.56042/ijbb.v62i7.16538

Exploring MHD convective based SWCNT-MWCNT-GO ternary hybrid nanofluids with variable viscosity and exothermic reactions

P Chandrakala* and V Srinivasa Rao

Department of Mathematics, Anurag University, Hyderabad-500 088, Telangana, India

Received 19 January 2025; *revised 20 February 2025*

The increasing demand for efficient thermal management in industrial applications, renewable energy systems, and advanced cooling technologies necessitates the development of high-performance heat transfer fluids. Ternary hybrid nanofluids, which combine multiple nanoparticles, offer a promising solution by enhancing heat and mass transfer properties beyond conventional fluids. This study investigates the convective heat and mass transfer characteristics of ethylene glycol-based ternary hybrid nanofluids composed of graphene oxide (GO), single-walled carbon nanotubes (SWCNTs), and multi-walled carbon nanotubes (MWCNTs) in a cylindrical annulus under non-uniform heat sources. The governing ordinary differential equations (ODEs) are formulated and numerically solved using MATLAB's Boundary Value Problem solver (BVP4c). Results indicate that increasing the nanoparticle volume fraction (ϕ) enhances the Nusselt number (Nu) by 15% and the Sherwood number (Sh) by 12%, significantly improving heat and mass transport. Additionally, a 20% increase in thermal efficiency is achieved with higher Grashof number (G) and magnetic parameter (M), while viscosity (B) and Eckert number (Ec) negatively impact transfer rates. These findings provide valuable insights for optimizing thermal systems, improving energy efficiency, and reducing operational costs in engineering applications.

Keywords: Activation energy, Entropy generation, Heat source, Heat transfer, Porous medium, Soret effect, Thermal conductivity

Nanofluids are a novel energy source that can be used by dispersing nanosized particles in conventional base fluids, due to recent advancements in nanotechnology and significantly boost the heat transfer coefficients and thermal conductivity of the base fluid. Choi and Eastman[1], were the first to introduce the idea of nanoparticles. Nanofluids, provide an enormous heat transmission because of their high thermal conductivity[2,4]. Despite their advantages, nanofluids face several challenges that must be addressed for practical applications. Stability and aggregation of nanoparticles remain major concerns, as these factors can lead to sedimentation and reduced thermal performance[5,6]. Additionally, viscosity and rheological behaviour significantly affect flow dynamics and energy consumption, as discussed by Namburu *et al*.[7] and Wang and Mujumdar[8]. Corrosion and compatibility with system materials also pose potential risks, as interactions between nanoparticles and metal surfaces can alter the integrity of heat exchangers and pipelines, as revealed by Singh *et al*.[9] and Keblinski *et al*.[10]. Furthermore, the scalability and cost-effectiveness of nanofluids remain critical factors in transitioning from laboratory research to large-scale industrial applications, as highlighted by Said *et al*.[11] and Sundar *et al*[12]. Addressing these challenges is essential to unlocking the full potential of nanofluids in thermal management applications.

Hybrid nanofluids, formed by dispersing multiple nanoparticles (metals, metal oxides, and carbon-based materials) into a base fluid, enhance thermal performance and heat transfer efficiency. Alkasasbeh and Mohamed[13] explored Williamson hybrid nanofluid flow over an exponential shrinking sheet in a porous medium, revealing the intricate interplay between magnetic fields, nanoparticle dispersion, and porous effects. Additionally, researchers developed a mathematical model of viscous and viscoelastic immiscible magnetohydrodynamic (MHD) fluid flow through a porous horizontal channel between two plates[14] and extended this concept to hybrid micropolar nanofluid flow over a solid sphere using computational modelling techniques.Building upon hybrid nanofluids, ternary nanofluids represent the next level of advancement in nanofluid technology, incorporating three distinct types of nanoparticles into a base fluid to further enhance thermal properties.

*Correspondence:
E-mail: chandrakalapanguluri@gmail.com

While hybrid nanofluids improve heat transfer by combining two different nanoparticles, ternary nanofluids introduce an additional nanoparticle, allowing for greater tunability of thermophysical properties and superior heat transfer performance. These fluids leverage the synergistic effects of multiple nanoparticles to optimize thermal conductivity, viscosity, and stability, making them highly promising for industrial and technological applications.

Shao *et al*. examined the natural convection behavior of ternary hybrid nanofluids in a porous prismatic chamber with heated moving barriers. Sahoo and Kumar analyzed the effects of temperature and volume fraction on Al_2O_3-CuO-TiO_2/water ternary nanofluids, while Mousavi *et al*. investigated the role of nanoparticle ratios in optimizing the thermophysical properties of CuO-MgO-TiO_2/water ternary nanofluids. These studies underscore the transition from hybrid to ternary nanofluids as a critical step in enhancing thermal management systems and advancing energy-efficient technologies.

Hybrid nanofluids, formed by dispersing multiple nanoparticles (metals, metal oxides, and carbon-based materials) into a base fluid, enhance thermal performance and heat transfer efficiency. Alkasasbeh and Mohamed[13] explored Williamson hybrid nanofluid flow over an exponential shrinking sheet in a porous medium, revealing the intricate interplay between magnetic fields, nanoparticle dispersion, and porous effects. Additionally, researchers developed a mathematical model of viscous and viscoelastic immiscible magnetohydrodynamic (MHD) fluid flow through a porous horizontal channel between two plates[14] and extended this concept to hybrid micropolar nanofluid flow over a solid sphere using computational modelling techniques. Ternary nanofluids represent a significant advancement in nanofluid technology, consisting of a base fluid infused with three distinct types of nanoparticles. These nanofluids have demonstrated superior heat transfer performance compared to both hybrid and mono nanofluids, making them highly promising for various industrial and technological applications. Shao *et al*.[15] examined the natural convection behavior of ternary hybrid nanofluids in a porous prismatic chamber with heated moving barriers. Sahoo and Kumar[16] examined the influence of temperature and volume fraction on Al_2O_3-CuO-TiO_2/water ternary nanofluids, and unlike their work, which attributed reduced heat transfer to low nanoparticle concentrations, this study identifies optimal conditions for improving thermal efficiency by adjusting Grashof numbers and magnetic parameters, achieving a 20% enhancement in thermal efficiency. In another study, the hydro-magneto-thermal behavior of ternary composite nanomaterial over an inclined thin needle, considering linear and nonlinear slip conditions, was investigated by Samantaray *et al.*[17]. Furthermore, Rashad *et al*.[18] focused on heat and mass transfer of Oldroyd-B and Jeffery-Williamson ternary hybrid nanofluids over a stretching sheet within a porous medium, providing insights into their thermal behavior and potential industrial applications.The results of this study reveal significant enhancements in heat and mass transfer rates, as evidenced by a 15% improvement in the Nusselt number and a 12% increase in the Sherwood number with increasing nanoparticle volume fraction. These findings align with earlier works by Choi and Eastman[1], who demonstrated improved thermal performance with nanoparticle dispersion, but go further by showing how ternary nanoparticles amplify these effects.

Graphite oxide (GO) and carbon nanotubes (CNTs) possess exceptional thermophysical properties, making them highly suitable for various industrial and engineering applications. Their superior mechanical strength and thermal conductivity enhance heat transfer performance compared to many other nanoparticles. Carbon nanotubes exist in two primary forms: single-walled carbon nanotubes (SWCNTs) and multi-walled carbon nanotubes (MWCNTs), both of which have been the focus of recent research. Due to their excellent electrical and structural properties, SWCNTs are particularly advantageous for applications in miniaturized electronic devices. Recent studies have also explored the influence of factors such as variable viscosity and activation energy on magnetohydrodynamic (MHD) convective heat transfer in cylindrical annuli[19] using ethylene glycol-based SWCNT and MWCNT nanofluids, further expanding their potential in thermal management systems. Regarding heat transfer phenomena, materials such as ethylene glycol, oils, and water tend to be low-conductivity. The effect of the hydromagnetic convective intensity movement stream of pivoting SWCNTs and MWCNT nanofluids in an upward channel with uneven thickness was explored in this study by Gopi[20].

Entropy generation, a key concept in the second law of thermodynamics, plays a crucial role in assessing

system inefficiencies due to energy losses from heat dissipation and friction. In real-world applications, achieving a perfectly efficient system without energy loss is unrealistic, prompting extensive research into energy dissipation. Analyzing entropy generation helps quantify irreversible losses in thermal processes, assess system disturbances, estimate capacity, and optimize efficiency[21]. Omid Mohain *et al*.[5] explored theoretical and computational aspects of entropy generation caused by heat transfer and nanofluid flow in various geometries and flow regimes.

The transformation of electrical energy into thermal energy has significant implications for heat transfer in the science of Joule heating. Joule heating increases the electrical conductivity, which improves the effectiveness of heat transfer. This phenomenon has found practical applications in a variety of fields, such as microdevices, electrical electronics, chemical reactors, and the petroleum and nuclear sectors. Joule heating affects fluid temperature, and temperature reduction is influenced by the Hartmann number[22,23].

There has been a significant dearth of research on the behavior of fluids enhanced by ternary nanoparticles, although the recent literature includes numerous studies on fluid flow between two concentric cylinders[24]. The significance of fluid flow and heat transmission in cylinders has increased due to scientific and industrial advancements. Several researchers have examined fluid flow in cylinders in light of this. Liu *et al*.[25] investigated the entropy and heat transfer produced by turbulent flow between concentric cylinders. Under boundary conditions involving wall deformation, Naveen Kumar *et al.*[26] investigated the flow behavior of a hybrid nanofluid driven by a rotating cone that was either stretching or shrinking. The annular cylinder geometry is considered in this study due to its practical relevance in various engineering applications, including heat exchangers, nuclear reactors, and cooling systems for high-performance electronics, where efficient heat and mass transfer is crucial. Its unique design provides an enhanced surface area compared to simple cylindrical configurations, improving thermal management performance. Additionally, the annular geometry introduces distinct flow characteristics due to the presence of both inner and outer boundaries, allowing for a more comprehensive analysis of buoyancy-driven flows, magnetic effects, and nanoparticle interactions. This configuration is also industrially significant, as it closely simulates real-world conditions in pipelines and cylindrical enclosures, making the findings highly applicable. Furthermore, existing literature predominantly focuses on simpler geometries like flat plates or single cylinders, and this study addresses that research gap by investigating the impact of annular configurations on thermal and hydrodynamic behaviour.

The fluid viscosity was taken as constant in the earlier research. It is crucial to understand that fluids' physical characteristics can change dramatically with temperature. This is especially important for lubricants because internal friction can produce heat, which raises the temperature and changes the fluid's viscosity and thermal conductivity[27]. Because of this aforementioned information, the fluid viscosity is assumed to be variable viscosity. The efficiency of heat transfer and convective flow is strongly impacted by the variable viscosity of the fluid, which is determined by the temperature and concentration of the nanoparticles. Existing studies on nanofluids have largely overlooked the combined effects of variable viscosity, exothermic chemical reactions, and activation energy on MHD convective heat transfer in cylindrical annuli, particularly for ternary hybrid nanofluids like ethylene glycol-based GO, SWCNTs, and MWCNTs (Table 1). These factors are crucial for improving the performance of heat exchangers, cooling systems, and other industrial applications where efficient thermal management is essential. This study addresses these gaps by analysing the influence of ternary nanoparticles, temperature-dependent heat sources, and complex chemical interactions on flow dynamics and heat transfer. By extending the Tiwari-Das[28] model to include variable viscosity and entropy generation, this work provides valuable insights into enhancing thermal efficiency and system performance under practical operating conditions. Moreover, this study addresses the limitations of existing literature by exploring the combined effects of activation energy, non-uniform heat sources, and exothermic chemical processes, which are often overlooked, to provide a comprehensive understanding of ternary nanofluids' superior thermal and mass transfer performance.

Table 1 — The thermophysical property values of the nanofluids

Nanofluid particles				Base fluid
Thermophysical properties	SWCNT	MWCNT	Go	Ethylene Glycol
Density(ρ), $kg.m^{-3}$	2600	1600	1800	1115
Specific heat Capacity (C_p) $JKg^{-1}k^{-1}$	425	706	717	2430
Thermal conductivity(k_f). $Wm^{-1}k^{-1}$	6600	3000	5000	0.253

This research seeks to address several key questions about advanced nanofluid systems:

- How do ternary nanoparticles affect the flow dynamics in concentric cylindrical annuli?
- How do temperature-dependent heat sources influence the flow and heat transfer properties of nanofluids?
- How does activation energy impact heat transfer and convective behavior, especially in the case of SWCNs, MWCNTs, and Go/Eg?

Mathematical formulation

This model examined the mixed convective flow of a ternary nanofluid based on ethylene (SWCNT+ MWCNT+GO/Eg) in a vertical circular annulus in porous media. This model Figure 1A assumes a linearly varying wall temperature along the axial direction (T_w=T_0+Az) to account for non-uniform heat sources, with heat generation/absorption considered uniformly distributed across the domain for mathematical simplicity. The cylindrical annulus configuration features inner and outer walls maintaining constant temperature and concentration gradients, with a homogeneous and isotropic porous medium ensuring uniform permeability and thermal conductivity. Despite these limitations, our study provides valuable insights into ternary nanofluid behavior in cylindrical annuli, with potential extensions to non-homogeneous porous structures, turbulent flow conditions, and more complex heat source distributions in future research.

The Boussinesq approximation is utilized to restrict density variations solely to thermal and molecular buoyancy effects, resulting in the coupling and nonlinearity of the momentum, energy, and diffusion equations.The axial flow of the cylindrical annulus is assumed to be unidirectional in this analysis. In these circumstances, the following governing equations are defined[19], taking into account the effects of exothermic chemical reactions:

$$-\frac{\partial p}{\partial z}+\frac{1}{\rho_{thnf}\delta r}\frac{\partial}{\partial r}\left(\mu_{thnf}(T)\,r\frac{\partial u}{\partial r}\right)-\left(\frac{\mu_{thnf}}{\rho_{thnf}k}\right)u-\frac{\sigma_{thnf}\mu_e^2H_0^2}{\rho_{thnf}r^2}-\frac{\delta F}{\rho_{thnf}\sqrt{k_p}}u^2+(\rho\beta)_{thnf}(T-T_o)=0 \quad \ldots (1)$$

$$(\rho C_p)_{thnf}\,u\frac{\partial T}{\partial z}=k_{thnf}\left(\frac{\partial^2T}{\partial r^2}+\frac{1}{r}\frac{\partial T}{\partial r}\right)+q'''-\frac{1}{r}\frac{\partial(rq_r)}{\partial r}+Q_e^*(C-C_0)Exp\left(-\frac{E_a}{K_pT}\right)+\mu_{thnf}(T)\left(\frac{\partial u}{\partial r}\right)^2+\sigma_{thnf}\mu_o^2H_o^2(u^2) \quad \ldots (2)$$

$$u\frac{\partial C}{\partial z}=D_B\left(\frac{\partial^2C}{\partial r^2}+\frac{1}{r}\frac{\partial C}{\partial r}\right)-k_c'C+\frac{D_mK_T}{T_s}\left(\frac{\partial^2T}{\partial r^2}+\frac{1}{r}\frac{\partial T}{\partial r}\right)-kc(\mathrm{C}-\mathrm{C}_0)\left(\frac{T}{T_o}\right)^nExp\left(-\frac{E_a}{K_pT}\right) \quad \ldots (3)$$

The temperature, fluid concentration, axial velocity in the porous media and porous medium permeability are denoted by T, C, u, and K respectively, and the thermal diffusivity, molecular diffusivity, mass diffusivity and mass diffusion coefficient are denoted by k_{thnf}, D_B, D_m, K_T respectively. Whereas F is a function that depends on the microstructure and Reynolds number of the porous medium, g is the gravitational acceleration, β is the thermal expansion, q_r is the radiation absorption coefficient, C_p is the specific heat, ρ represents the density, ρ_{thnf} is the ternary nanofluid's density, μ_{thnf} is its dynamic viscosity, and σ_{thnf} is its thermal conductivity.

The dynamic viscosity of the nanofluids is assumed to be temperature dependent as follows[30]:

$$\mu_{thnf}(T)=\mu_{thnf}Exp(-m(T-T_0)) \quad \ldots (4)$$

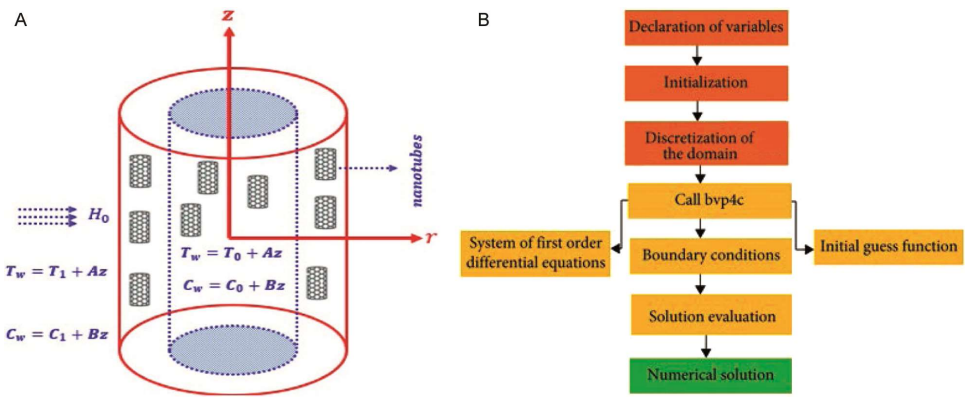

Fig. 1 — (A) Configuration of the flow geometry; and (B) BVP4c flow chart

At μ_{thnf} is the nanofluid viscosity at ambient temperature T_0 and m is the viscosity variation parameter, which depends on the particular fluid.

The relevant boundary conditions are:

$u = 0$,T=T_w,C=$C_w$atr = a & a+s ... (5)

According to Das *et al.* [28]and Tao[29], the temperature and concentration at both walls are expressed as follows:

$$T_w = T_0 + Az \ , \quad C_w = C_0 + Bz$$

The vertical temperature and concentration gradients are represented by A and B, respectively. In buoyancy-assisted flow, A is positive, whereas B is positive for buoyancy-opposed flow. The upstream reference temperature is denoted as T_0, and the upstream reference concentration is C_0. The internal heat generation rate is characterized by the coefficient and is mathematically expressed as[29]:

$$q''' = (\frac{k_{thf}}{a^2 \nu})(A_{11}(T_w - T_0)u + B_{11}(T - T_0) \quad \text{... (6)}$$

Where A_{11} and B_{11} are the coefficients for space-dependent and temperature-dependent internal heat generation or absorption, respectively. It should be noted that

- For A_{11} >0 and B_{11} >0, the scenario corresponds to internal heat generation.
- Conversely, if A_{11} <0 and B_{11} <0, the scenario corresponds to internal heat absorption.

For a laminar flow subjected to a radial magnetic field, the temperature and concentration distributions within the fluid are dependent on the radial and vertical coordinates, r and z, respectively. All other physical variables, such as pressure, temperature, and concentration, vary as functions of r and z, while the velocity is exclusively a function of the radial coordinate, r.

$$T = T^{\bullet}(r) + Az \quad , \quad C = C^{\bullet}(r) + Bz \quad \text{... (7)}$$

The effective thermophysical properties are defined by Usman *et al*.[31]

Ternary nanofluids

$$\mu_{thnf} = \frac{\mu_f}{\left(1-(\phi_1+\phi_2+\phi_3)\right)^{2.5}}$$

$$\rho_{thnf} = (1-(\phi_1+\phi_2+\phi_3))\rho_f + \phi_1\rho_{s1} + \phi_2\rho_{s2} + \phi_3\rho_{s3}$$

$$(\rho c_p)_{thnf} = (1-(\phi_1+\phi_2+\phi_3))(\rho c_p)_f + \phi_1(\rho c_p)_{s1} + \phi_2(\rho c_p)_{s2} + \phi_3(\rho c_p)_{s3}$$

$$(\rho\beta)_{thnf} = (1-(\phi_1+\phi_2+\phi_3))(\rho\beta)_f + \phi_1(\rho\beta)_{s1} + \phi_2(\rho\beta)_{s2} + \phi_3(\rho\beta)_{s3}$$

$$\frac{k_{thnf}}{k_f} = \frac{\phi_1 k_1 + \phi_2 k_2 + \phi_3 k_3 + 2(\phi_1+\phi_2+\phi_3)k_f + 2(\phi_1+\phi_2+\phi_3)}{\phi_1 k_1 + \phi_2 k_2 + \phi_3 k_3 + 2(\phi_1+\phi_2+\phi_3)k_f - (\phi_1+\phi_2+\phi_3)}$$

Hybrid nanofluids

$$\mu_{hnf} = \frac{\mu_f}{\left(1-(\phi_1+\phi_2)\right)^{2.5}}$$

$$\rho_{hnf} = (1-(\phi_1+\phi_2))\rho_f + \phi_1\rho_{s1} + \phi_2\rho_{s2}$$

$$(\rho c_p)_{hnf} = (1-(\phi_1+\phi_2))(\rho c_p)_f + \phi_1(\rho c_p)_{s1} + \phi_2(\rho c_p)_{s2}$$

$$(\rho\beta)_{hnf} = (1-(\phi_1+\phi_2))(\rho\beta)_f + \phi_1(\rho\beta)_{s1} + \phi_2(\rho\beta)_{s2}$$

$$\frac{k_{hnf}}{k_f} = \frac{\phi_1 k_1 + \phi_2 k_2 + 2(\phi_1+\phi_2)k_f + 2(\phi_1+\phi_2)(\phi_1 k_1 + \phi_2 k_2) - 2(\phi_1+\phi_2)^2 k_f}{\phi_1 k_1 + \phi_2 k_2 + 2(\phi_1+\phi_2)k_f - (\phi_1+\phi_2)(\phi_1 k_1 + \phi_2 k_2) + (\phi_1+\phi_2)^2 k_f}$$

Nanofluids

$$\mu_{nf} = \frac{\mu_f}{\left(1-(\phi_1)\right)^{2.5}}$$

$$\rho_{nf} = (1-(\phi_1))\rho_f + \phi_1\rho_{s1}$$

$$(\rho c_p)_{nf} = (1-(\phi_1))(\rho c_p)_f + \phi_1(\rho c_p)_{s1}$$

$$(\rho\beta)_{nf} = (1-(\phi_1))(\rho\beta)_f + \phi_1(\rho\beta)_{s1}$$

$$\frac{k_{nf}}{k_f} = \frac{\phi_1 k_1 + \phi_2 k_2 + 2(\phi_1)k_f + 2(\phi_1)(\phi_1 k_1) - 2(\phi_1)^2 k_f}{\phi_1 k_1 + 2(\phi_1)k_f - (\phi_1)(\phi_1 k_1) + (\phi_1)^2 k_f}$$

where $(\ )_{thnf}$, $(\ )_{hnf}$, $(\ )_{nf}$ represent ternary nanofluids, hybrid nanofluids and mono nanofluids, respectively.

The following nondimensional variables were defined for the analysis:

$$z^* = \frac{z}{a} \ r^* = \frac{r}{a} \ u^* = (\frac{a}{\nu})u \ , \ p^* = \frac{pa\delta}{\rho\nu^2} \ ,$$

$$\theta^*(r^{\bullet}) = \frac{T^{\bullet} - T_0}{P_1 Aa} \quad , \quad \Phi^*(r^{\bullet}) = \frac{\Phi^{\bullet} - \Phi_0}{P_1 Ba} \ ,$$

$$s^* = \frac{s}{a}, P_1 = \frac{dp}{dx} \quad \text{... (8)}$$

$$A_1 = \left(1-(\phi_1+\phi_2+\phi_3)\right)^{2.5}$$

$$A_2 = \left(1-(\phi_1+\phi_2+\phi_3)\right) + \phi_1(\frac{\rho_1}{\rho_f}) + \phi_2(\frac{\rho_2}{\rho_f}) + \phi_3(\frac{\rho_3}{\rho_f})$$

$$A_3 = \left(1-(\phi_1+\phi_2+\phi_3)\right) + \phi_1(\frac{\rho_1\beta_1}{\rho_f}) + \phi_2(\frac{\rho_2\beta_2}{\rho_f}) + \phi_3(\frac{\rho_3\beta_3}{\rho_f})$$

$$A_4 = \left(1-(\phi_1+\phi_2+\phi_3)\right) + \phi_1(\frac{\rho_1 c_p}{\rho_f}) + \phi_2(\frac{\rho_2 c_p}{\rho_f}) + \phi_3(\frac{\rho_3 c_p}{\rho_f})$$

$$A_5 = \frac{k_{thnf}}{k_f}$$

$$A_6 = (1 + \frac{3(\sigma-1)}{\sigma+2-(\sigma-1)\phi}), \sigma_{thnf} = \sigma_f A_6, \ \sigma = \frac{\sigma_s}{\sigma_f}$$

Introducing these nondimensional variables, the governing equations in nondimensional form are (on removing the stars)

$$(\frac{\partial^2 u}{\partial r^2}+\frac{1}{r}\frac{\partial u}{\partial r}-\mathrm{B}(\frac{\partial u}{\partial r})(\frac{\partial T}{\partial r}))=A_1A_3\,\mathrm{e}^{\mathrm{B}\theta}+\delta A_1(K+\frac{A_6M^2\,\mathrm{e}^{B\theta}}{r^2})u-Fr(u^2)+\delta A_1A_4G\,\mathrm{e}^{\mathrm{B}\theta}(\theta) \quad \text{... (9)}$$

$$(\mathrm{A}_5+\frac{4Rd}{3})(\frac{\partial^2\theta}{\partial r^2}+\frac{1}{r}\frac{\partial\theta}{\partial r})+\mathrm{Pr}(A_{11}u+B_{11}\theta)+Q_1.\mathrm{Pr}.Ce^{-(\frac{E}{1+\delta\theta})}+Ec.\mathrm{Pr}.\mathrm{e}^{-\mathrm{B}\theta}(\frac{\partial u}{\partial r})^2+$$
$$+Ec.\mathrm{Pr}.\mathrm{A}_6M(u^2)=A_4\,\mathrm{Pr}.u \quad \text{... (10)}$$

$$(\frac{\partial^2\Phi}{\partial r^2}+\frac{1}{r}\frac{\partial\Phi}{\partial r})-\gamma.\Phi(1+n\delta\theta)Exp(-\frac{E}{1+\delta\theta})=Sc.u+Sc.Sr\left(\frac{\partial^2\theta}{\partial r^2}+\frac{1}{r}\frac{\partial\theta}{\partial r}\right) \quad \text{... (11)}$$

where

$\mathrm{B}=m(T_0-T_i)$ is the viscosity parameter

$Fr=F\sqrt{K_p}$ is the inertia parameter or Forchheimer number

Where $\Delta=\mathrm{FD}^{-1/2}$ (Inertia parameter or Forchheimer number), $G=\frac{g\beta(T_e-T_i)a^3}{\nu^2}$ is the Grashof number, $M^2=\frac{\sigma\mu_e^2H_0^2}{a\nu}$ is the magnetic parameter, $K=\frac{a^2}{k}$ is the inverse Darcy parameter, $\mathrm{Pr}=\frac{\mu C_p}{k_f}$ is the Prandtl number, $Rd=\frac{4\sigma^{\bullet}T_o^3}{k_{thnf}\beta_R}$ is the thermal radiation parameter, $Sc=\frac{\nu}{D_B}$ is the Schmidt number, $\gamma=\frac{k_ca^2}{D_B}$ is the chemical reaction parameter, $Sr=\frac{D_mK_T(T_0-T_{i)}}{T_s(C_0-C_i)}$ is the Soret parameter, $Q_1=\frac{Q_e^*(C_w-C_0)}{a^2(T_w-T_0)}$ is the radiation absorption parameter, $\delta=\frac{T_w-T_\infty}{T_\infty}$ is the temperature difference ratio where $\theta_w=\frac{T}{T_o}$, $\mathrm{E}=\frac{\mathrm{E}}{K_pT\infty}$ is the activation energy parameter, $Ec=\frac{u^2\rho_f}{\left(\rho C_p\right)_f\left(T_w-T_\infty\right)}$ is Eckert number and $D^{-1}=\mathrm{a}^2/k$ inverse Darcy parameter.

The corresponding non-dimensional conditions are:

$u=0 \quad \theta=0 \quad \Phi$=0atr=1 and 1+s ... (12)

Analysis of Entropy generation and Bejan number

Heat transfer resulting from temperature gradients, viscous dissipation from fluid friction, and concentration gradients of nanoparticles are the sources of the local volumetric rate of entropy generation in nanofluid flows. It is feasible to lower entropy generation and enhance thermal performance in such systems by optimizing these parameters:

$$s'''=\frac{k_{thnf}}{T_0^2}\left(\frac{\partial T}{\partial y}\right)^2+\frac{\mu_{thnf}(T)}{\Delta T_0}\left(\frac{\partial u}{\partial y}\right)^2+\frac{\sigma_{thnf}B_0^2u^2}{\Delta T_0}+\frac{D_B}{\Delta T_0}(\left(\frac{\partial T}{\partial y}\right))^2+\frac{D_B}{\Delta T_0}\left(\frac{\partial T}{\partial y}\right)\left(\frac{\partial\Phi}{\partial y}\right)$$

In non-dimensional form,

$$N_s=\frac{a^2s'''}{k_{thnf}}=\left(\frac{\partial\theta}{\partial\eta}\right)^2+Br[e^{-B\theta}\left(\frac{\partial u}{\partial\eta}\right)^2+M(u^2)+\lambda\left[\left(\frac{\partial\theta}{\partial\eta}\right)^2+\left(\frac{\partial\theta}{\partial\eta}\right)\left(\frac{\partial\Phi}{\partial\eta}\right)\right]$$

where

$Br=Ec.\mathrm{Pr}(Brinkman\ number)$, $\lambda=\frac{\Phi_0D_B}{k_{thnf}}$ mass transfer parameter

$$N_1=\left(\frac{\partial\theta}{\partial\eta}\right)^2, N_2=Br[e^{-B\theta}\left(\frac{\partial u}{\partial\eta}\right)^2+M(u^2)$$

$$N_3=\lambda\left[H_n^2+H_n\theta_n\right]$$

Irreversibility ratio is defined by

$$\chi=\frac{N_2}{N_1+N_3}$$

Heat and nano particles mass transfer irreversibility dominates for $0\le\chi\le1$ and fluid friction irreversibility dominates when $\chi>1$. The concentrations of both irreversibilities to entropy generation are equal when $\chi=1$.

Here, $Be=\frac{N_1+N_3}{N_2}=\frac{1}{1+\chi}$ is the Bejan number (Be)

Be has a range of 0 to 1. Be=1 is the limit where the irreversibility resulting from heat and nanoparticle mass transfer dominates the flow systems, whereas this is the limit where the effect of fluid friction dominates irreversibility. When Be=1/2, there is no difference in the irreversibilities of heat and mass transfer and fluid friction.

Solution procedure

The bvp4c solver in MATLAB (as in Fig. 1B) was used to solve the nonlinear ordinary differential equation (ODE) system (9–11) and the accompanying boundary conditions (12). The numerical computations in this study were carried out using the BVP4c solver in MATLAB, which is well-suited for solving boundary value problems with high accuracy. The governing equations and boundary conditions were discretized over a uniform mesh with a step size of Δr=0.01. The step size was chosen to meet a convergence criterion where the results (*e.g,* velocity, temperature, and concentration profiles) achieved

consistency with six decimal places of accuracy. Smaller step sizes were tested iteratively until the desired level of precision was reached. The stability of the numerical method (*e.g,* BVP4c in MATLAB) was a key consideration. The step size was adjusted to avoid numerical oscillations or divergence during computations. The serves as a convergence requirement to obtain a solution with six decimal places of accuracy. The parameters in this study include Grashof number (G = 10), magnetic field parameter (M = 0.5), nanoparticle volume fraction ($\phi = 0.05$), and other parameters within specified ranges.

Equations (9–11) need to be coded by considering:

$$f = y_{1,}\ f' = y_2,\ \mathrm{f}'' = \mathrm{y}_{3,} f''' = y_4,$$
$$\theta = y_5,\ \theta' = \mathrm{y}_{6,}\ \theta'' = y_7$$
$$\Phi = y_8,\ \Phi' = \mathrm{y}_9,\ \Phi'' = \mathrm{y}_{10}$$

The following formulas are used to compute the shear stress (τ), the rate of heat transfer (Nusselt number Nu), and the rate of mass transfer (Sherwood number Sh).

$$\tau = (\frac{du}{dr})_{r=1,1+s}\ )\ Nu = -(\frac{d\theta}{dr})_{r=1,1+s} \cdot Sh = -(\frac{d\Phi}{dr})_{r=1,1+s}$$

The values presented in Table 2 were computed by solving the governing equations numerically using the boundary value problem solver (BVP4c) in MATLAB. To ensure accuracy and validation, the results were first compared with existing studies that investigated mono nanofluids under similar conditions. For a mono nanofluid with E=0 and B=0, the results show good agreement with those of Kiran Kumar *et al*[32].

Graphical analysis

This study examines how variable viscosity, activation energy, chemical reactions, and nonuniform heat sources influence nanofluid behavior under MHD convective conditions, offering insights into their engineering applications.

Effects on velocity profiles

Figures 2A and 3A shows that increasing nanoparticle volume fraction (ϕ) and Grashof number G causes a rise in fluid velocity u. A higher Grashof number increases buoyant forces, allowing for easier fluid movement. Figures 4A and 5A show variations in velocity profile against inverse Darcy parameter (K) and magnetic parameter (M).

Figure 6A illustrates variations in velocity profile against Forchheimer parameter (Fr). A higher Forchheimer number Fr corresponds to a slower decrease in f′(η), indicating a less rapid reduction in velocity. Because of the increased surface porosity, there is less liquid mobility, which impacts the Forchheimer number (Fr). Figure 7A illustrates the impact of viscosity (B) on fluid velocity (u), showing that as B increases, the boundary layer thickens, and fluid density decreases. Figure 8A depicts the relationship between fluid velocity (u) and the Eckert number (Ec), where increasing Ec reduces velocity due to higher energy dissipation converting kinetic energy into heat, thereby slowing fluid momentum.

Effects on Temperature Profiles

Figure 2B illustrates the rise in fluid temperature with rise volume fraction (ϕ) for different nanoparticles SWCNT+MWCNT+GO-Eg, MWCNT+ GO-Eg, and GO-Eg, in a vertical circular channel. Whereas greater Grashof numbers (G) and magnetic parameters (M) also improve the temperature profiles, as shown in (Fig. 3B). A higher magnetic parameter (M) suppresses turbulence and stabilizes the flow, while an increased Grashof number (G) enhances natural convection by strengthening buoyancy forces. Figure 9A depicts the effect of the radiation parameter (Rd) on the temperature profile. The decrease in fluid temperature is observed regardless of the presence of nanofluids, with enhanced Rd behavior consistently accelerating the reduction in temperature. Thermal radiation and heat absorption boost the thermal profile and energy transmission rates by allowing efficient energy transfer through electromagnetic waves, creating steeper temperature gradients. Ternary nanofluids exhibit the highest followed by hybrid and mono nanofluids.

Table 2 — Code Validation

Parameter		Kumar *et al.*[26] results		Present Results		Kumar *et al*[26]		Present Results	
		Ethylene Glycol -Swcnt				Ethylene Glycol -Mwcnt			
		τ (1)	Nu (1)	τ (1)	Nu (1)	τ (1)	Nu (1)	τ (1)	Nu (1)
Rd	0.5	-0.167073	0.999967	-0.167074	0.999970	-0.102190	0.999954	-0.102191	0.999956
	1.5	-0.167075	0.999992	-0.167076	0.999995	-0.102192	0.999976	-0.102195	0.999975
Ec	0.01	-0.334341	0.999953	-0.334342	0.999952	-0.102191	0.999955	-0.102192	0.999957
	0.03	-0.167074	0.999965	-0.167075	0.999965	-0.102190	0.999951	-0.102190	0.999951

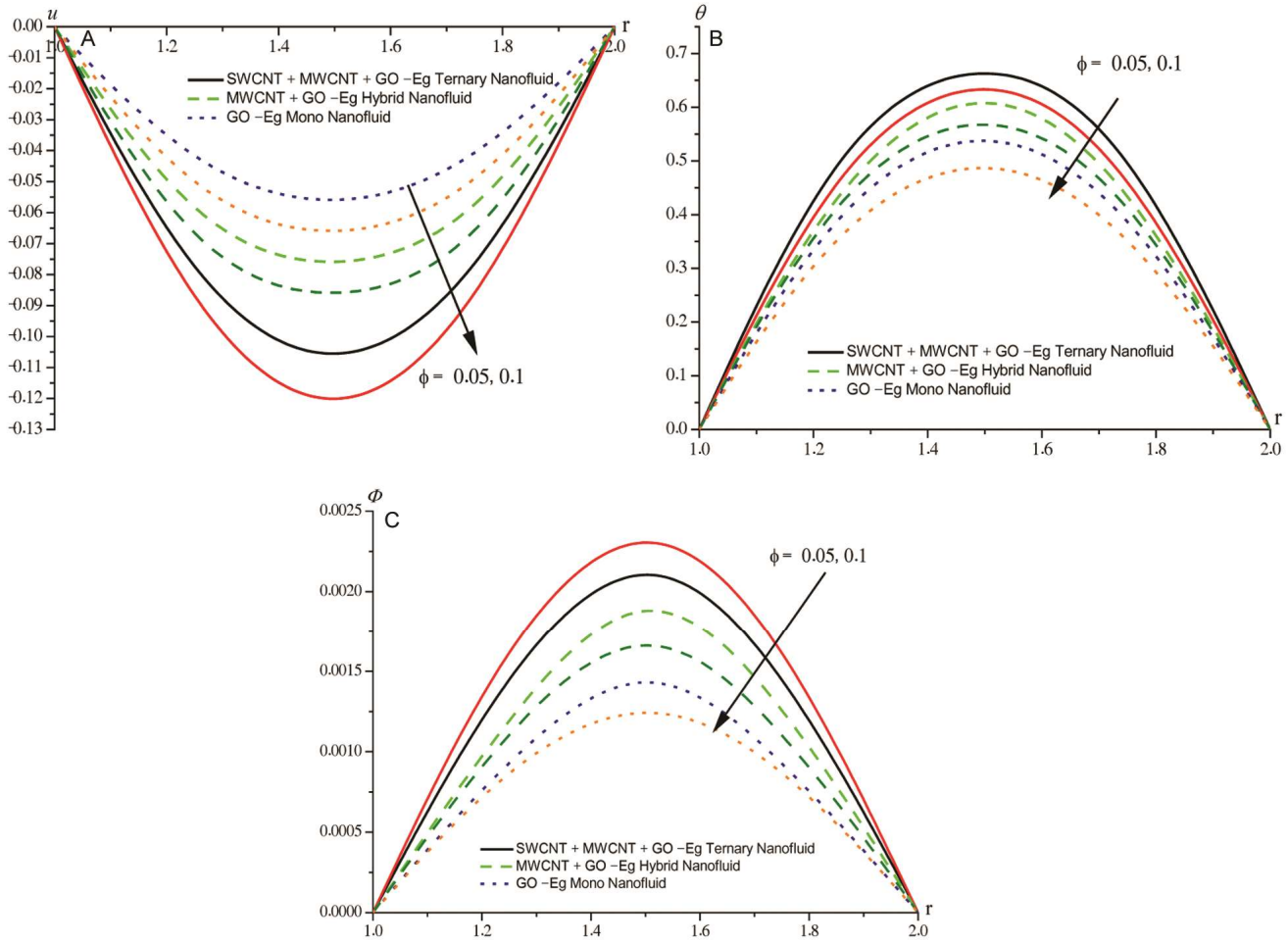

Fig. 2 — (A) ϕ *vs* velocity (u); (B) ϕ *vs* temperature (θ); and (C) ϕ *vs* nanoconcentration (Φ)

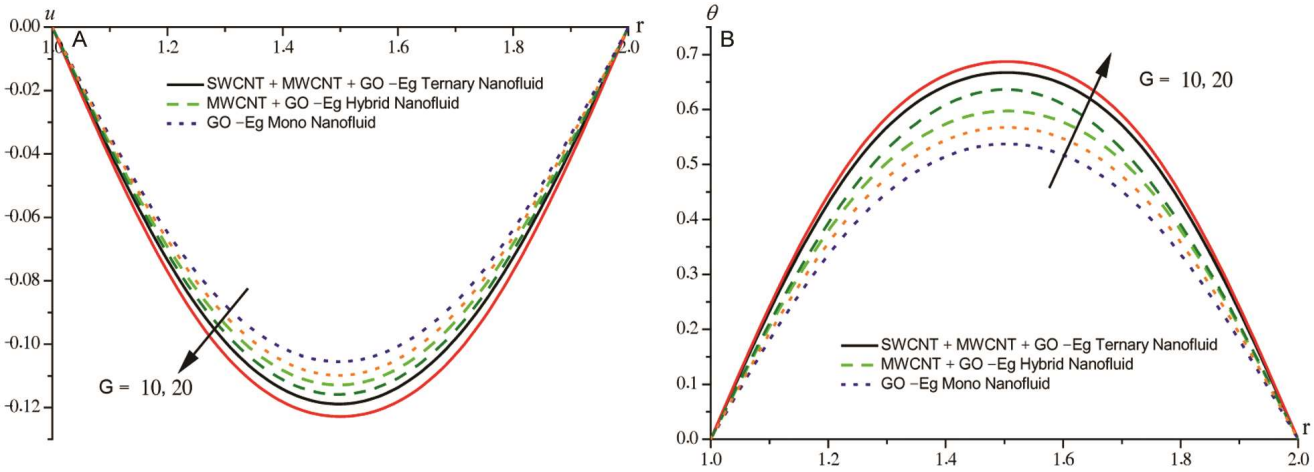

Fig. 3 — (A) G *vs* Velocity (*u*); and (B) G *vs* Temperature (θ)

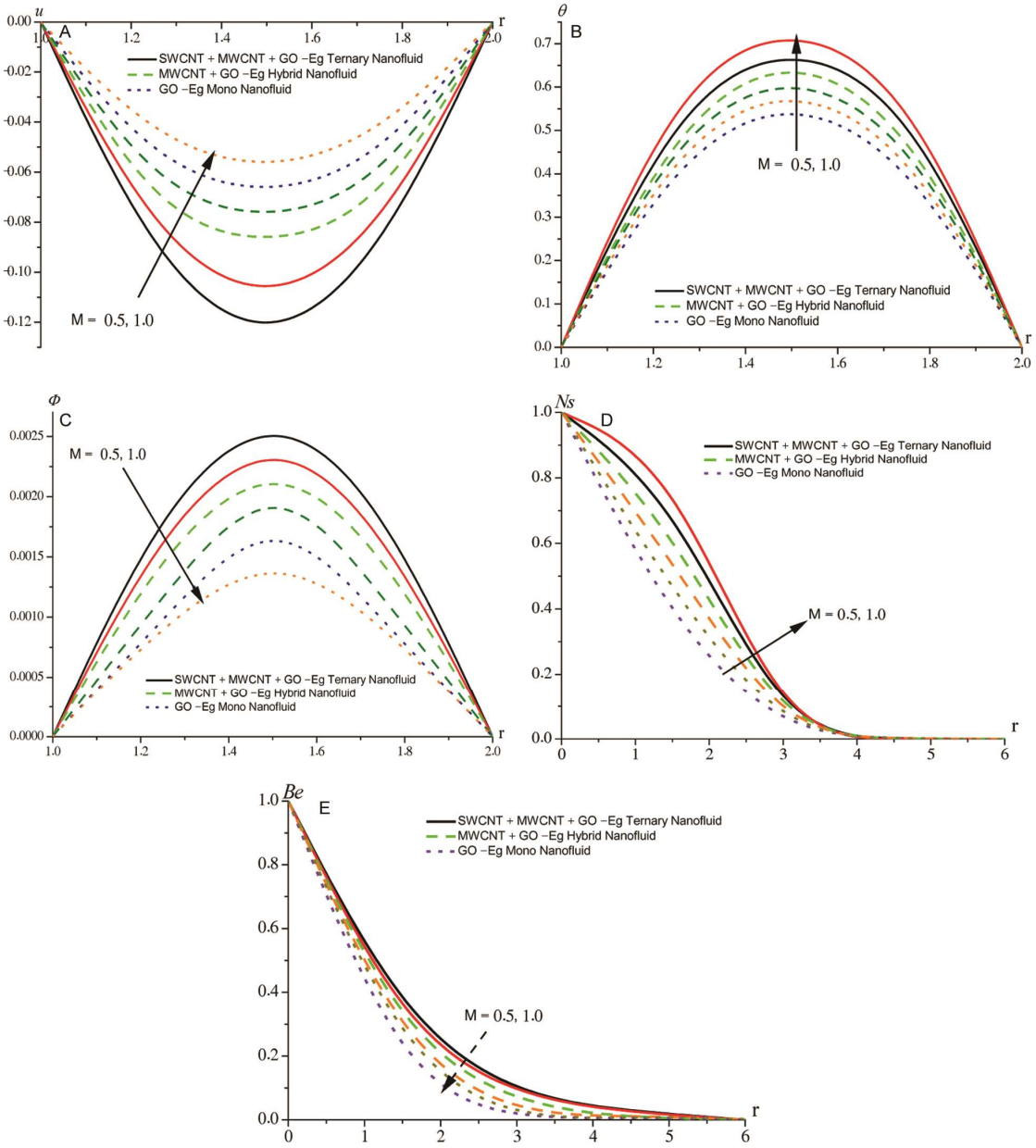

Fig. 4 — (A) M *vs* velocity(u); (B) M *vs* θ; (C) M *vs* Φ; (D) M *vs* Ns; and (E) M *vs* Be

Figure 10A shows that the temperature profile decreases as Pr increases. Figures 11A-13A illustrates the effect of temperature profile on Soret number (Sr). Schmidt number (Sc), and chemical reaction parameter (γ) for different nanofluids. The Soret number (Sr) increases the temperature profile because particle movement into hotter regions strengthens local temperatures. The Schmidt number (Sc) reduces thermal dispersion and affects the temperature profile by decreasing mass diffusion, which is related to momentum transfer.

Figure 16A depicts the temperature reading for Q1. Increasing Q_1 enhances energy transfer, rising temperature, and boundary layer thickness.The effect of activation energy (Ea) on the performance of various nanofluid compositions is shown in (Fig. 17A). The maximum peak is reached by the ternary nanofluid, which is followed by the hybrid and mono nanofluids (GO).

Effects on nanoparticle concentration profiles

As seen in Figures 11C-15C, lower nanoparticle concentrations are obtained with greater Soret number

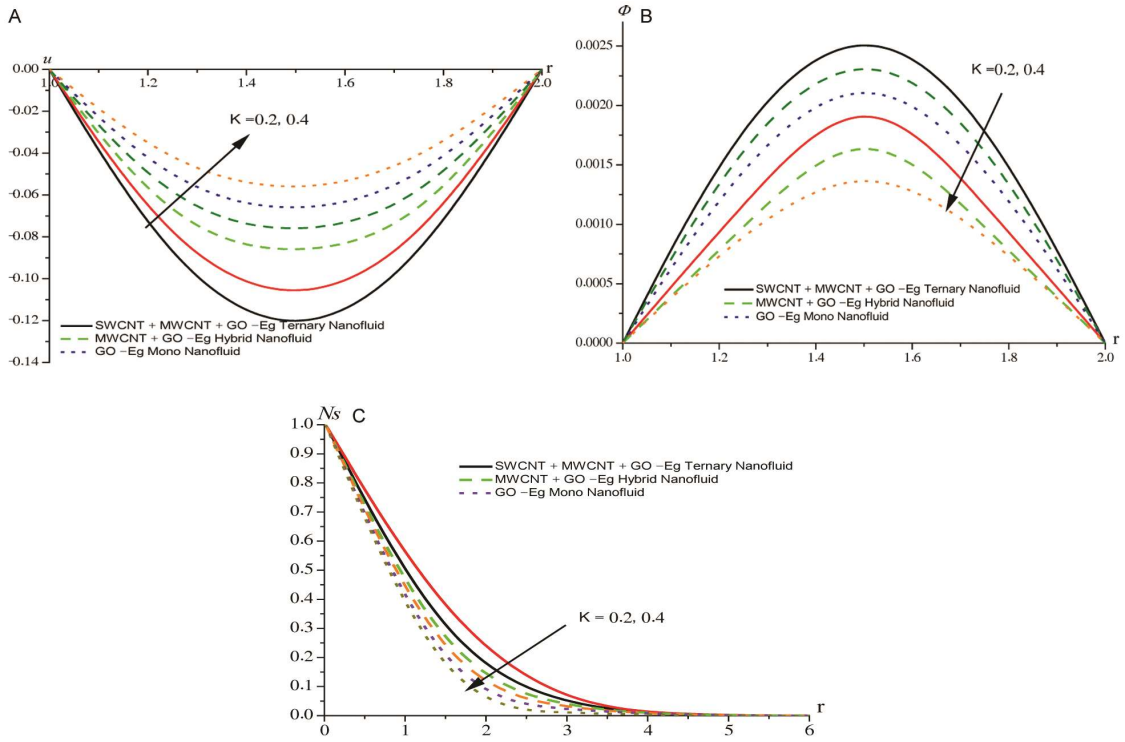

Fig. 5 — (A) K *vs* velocity(u); (B) K *vs* Φ; and (C) K *vs* Ns

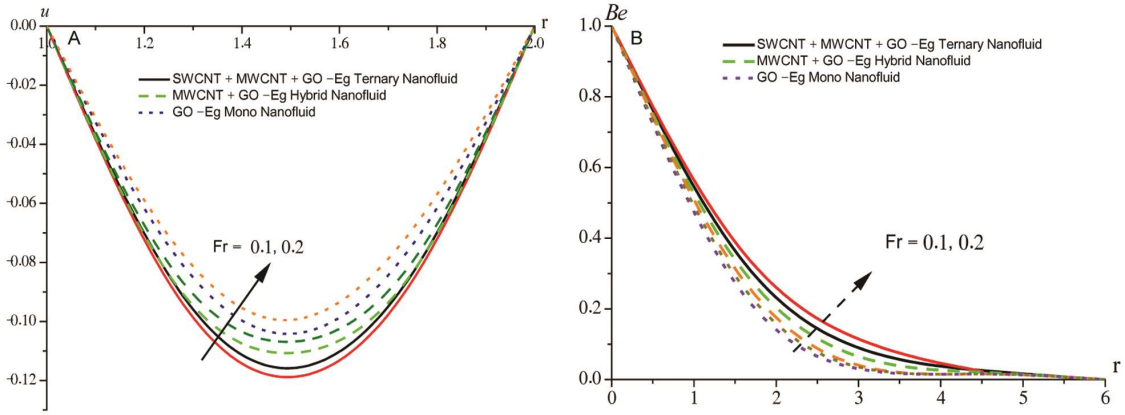

Fig. 6 — (A) Fr *vs* velocity (u); and (B) Fr *vs* Be

(Sr) and heat source parameters (A_{11} and B_{11}). As seen in Fig. 15B, the activation energy (Ea) raises the concentration. A higher activation energy causes the rate of chemical reactions to slow down and consume fewer reactants, accumulating particles and raising the concentration profile as a result. This is important in catalytic reactors and energy storage systems, where the rate of reaction needs to be optimized for efficient energy conversion and storage.

Effects on Entropy Generation Analysis:

Figure 4D shows that as the magnetic parameter M increases, entropy generation rises near the inner cylinder and decreases near the outer cylinder, highlighting the impact of M in thermodynamic inefficiencies by affecting fluid friction and heat transfer, with reduced entropy generation near the inner cylinder suggesting that lowering M could be beneficial, especially in applications like nuclear MHD propulsion.

Figures 7C and 8C show the correlation between the thermal radiation parameter Rd, viscosity parameter B, and entropy generation Ns.As Rd and B increase, entropy generation decreases near the inner cylinder (r = 1), suggesting that stronger thermal radiation and higher viscosity lead to a more organized flow, which reduces entropy production. In

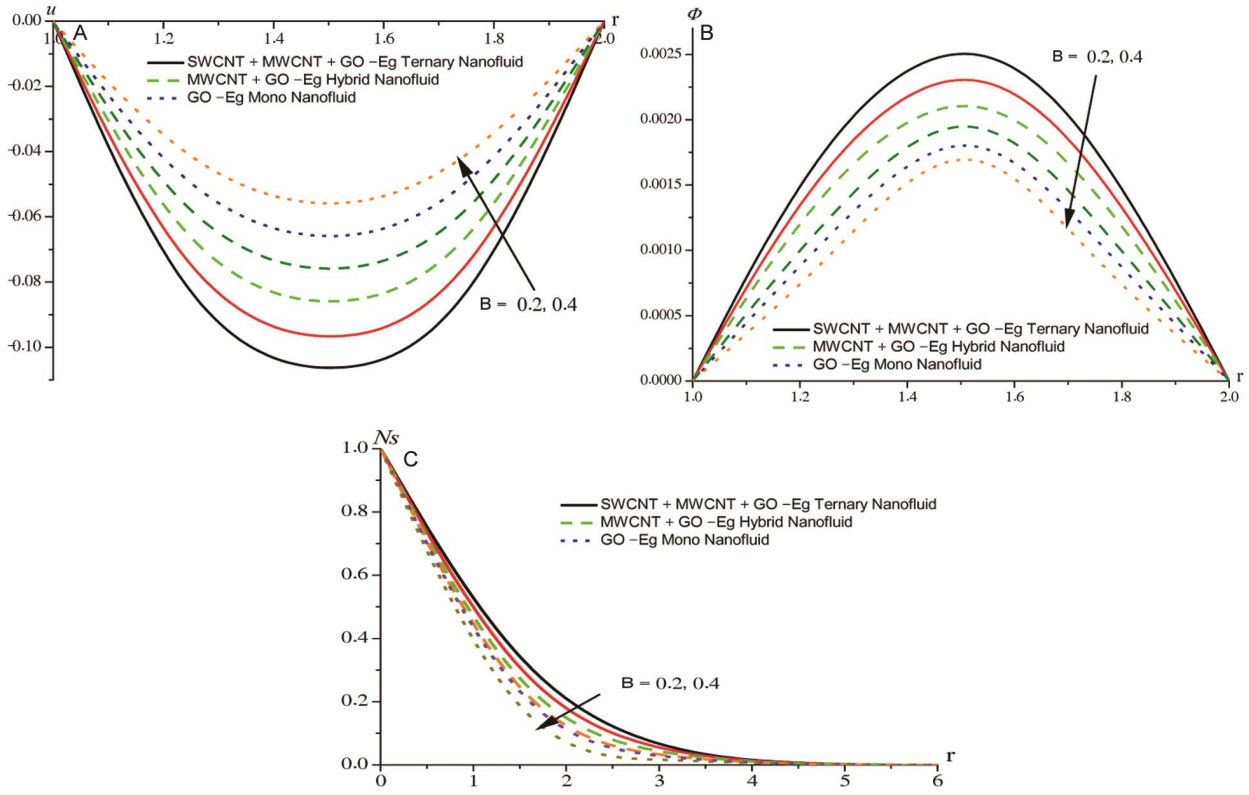

Fig. 7 — (A) B *vs* velocity (u); (B) B *vs* Φ; and (C) B *vs* Ns

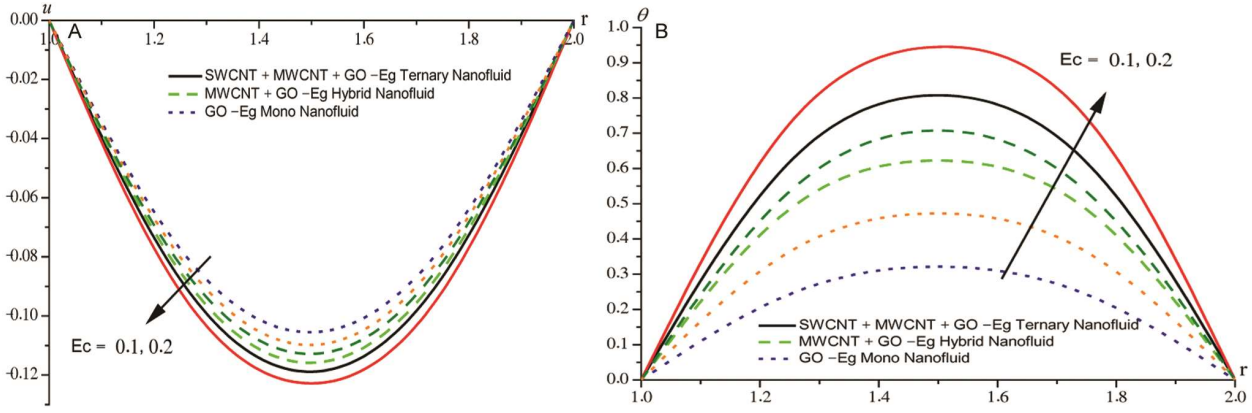

Fig. 8 — (A) Ec *vs* velocity (u); and (B) Ec *vs* θ

Figures 14A and 15A, it is observed that increasing the heat source parameters (B11) and (A11) lowers entropy generation near the inner cylinder, with the effect levelling off at r = 2. This suggests that greater heat sources improve heat transport, resulting in lower entropy generation, especially as the fluid flows away from the inner cylinder.

Figure 16B demonstrates how radiation absorption, characterized by the parameter Q1, impacts entropy generation. As radiation absorption increases, thermal irreversibilities become more pronounced, leading to greater entropy generation, particularly near the heated surface. Figure 17A reveals that increasing activation energy (Ea) promotes more chemical reactions, resulting in higher entropy generation near the inner cylinder. In contrast, Figure 18B shows that as the mass transfer parameter (λ) grows, entropy generation falls toward the inner cylinder, with a small impact on the outside boundary. Higher values of the parameter (λ) reduce entropy generation near

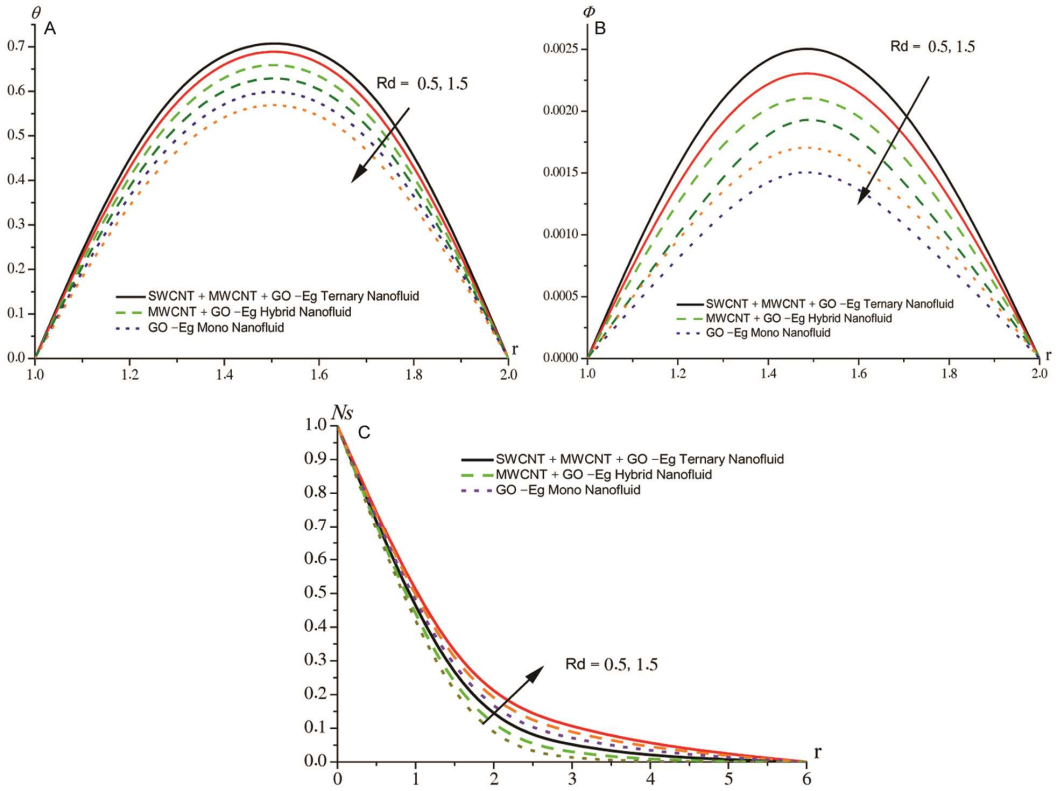

Fig. 9 — (A) Rd *vs* θ; (B) Rd *vs* Φ; and (C) Rd *vs* Ns

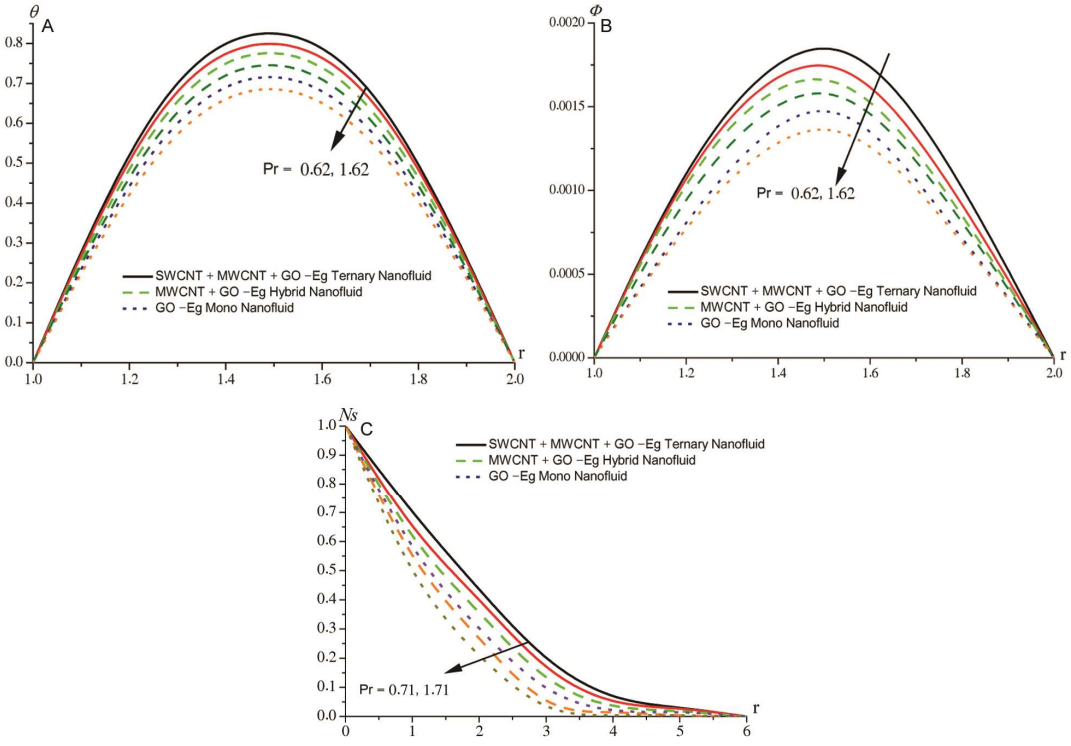

Fig. 10 — (A) Pr *vs* θ; (B) Pr on Φ; and (C) Pr *vs* Ns

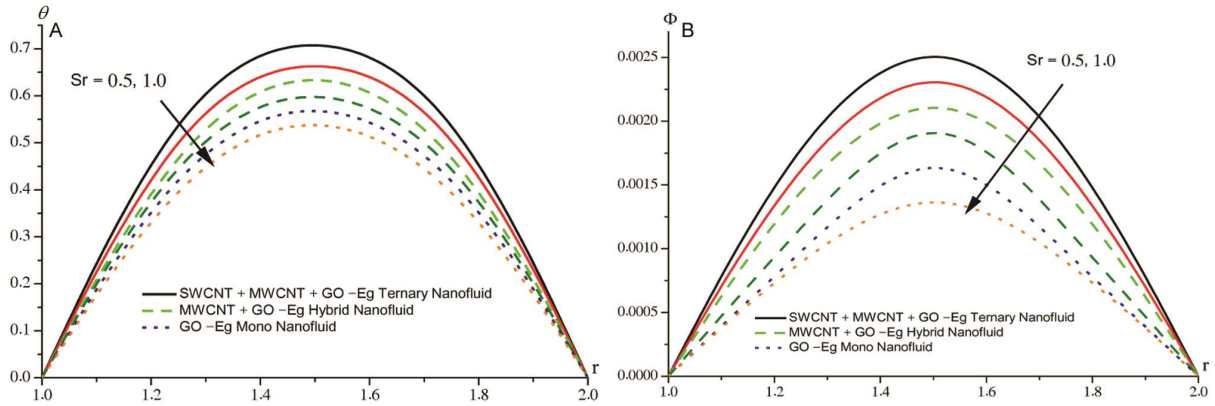

Fig. 11 — (A) Sr *vs* θ; and (B) Sr *vs* Φ

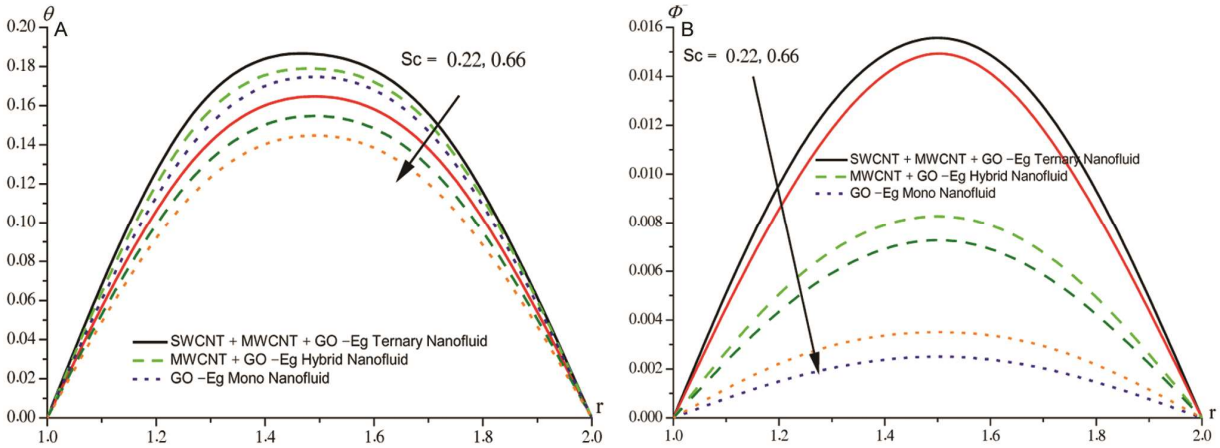

Fig. 12 — (A) Sc *vs* θ; and (B) Sc *vs* Φ

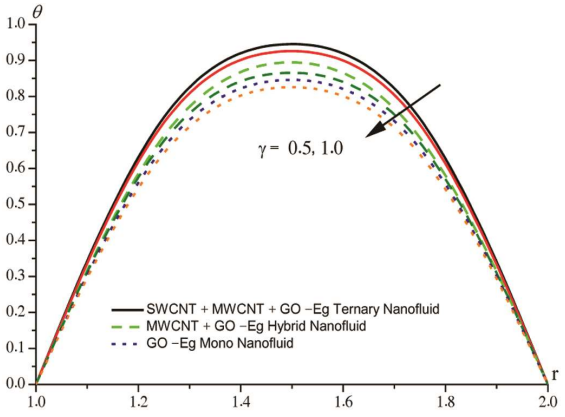

Fig. 13 — γ *vs* θ

the cylinder. Higher values of the parameter δ1 lead to a reduction in entropy generation near the cylinder, with minimal effects farther from the surface.

Figure 19 shows how the Brinkman number (Br) affects entropy generation (Ns). As Br increases, flow resistance rises due to more viscous dissipation, which boosts the concentration of nanoparticles. This leads to higher entropy generation because stronger viscous forces and a greater number of nanoparticles cause more energy to be lost as heat.

Effects on the Bejan Number

Figures 2E and 4E show that increasing the nanoparticle volume fraction (ϕ) or magnetic parameter (M) lowers the Bejan number near the inner cylinder, as heat transfer becomes more important than fluid friction in generating entropy. Figures 14B and 15B show that increasing the space-dependent (A11) and temperature-dependent (B11) heat source parameters raises the Bejan number, meaning stronger heat sources near the inner cylinder create more entropy from heat transfer. Figures 17 and 18C show that higher values of activation energy (Ea) and temperature ratio (δ1) decrease the Bejan number near r=1, indicating that heat transfer becomes more dominant and fluid friction contributes less to entropy generation. Overall, Be near the inner

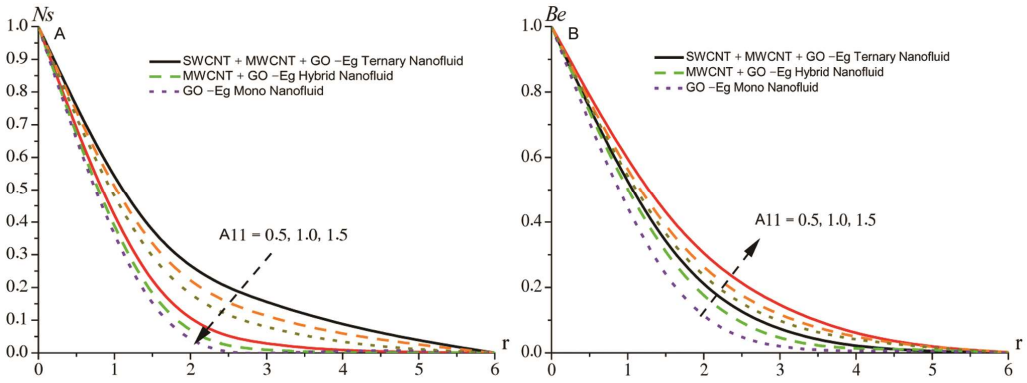

Fig. 14 — (A) A_{11} *vs* Ns; and (B) A_{11} *vs* Be

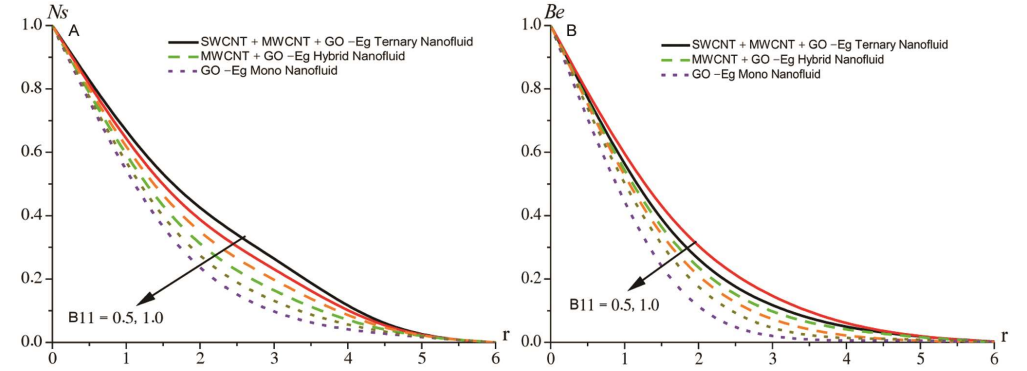

Fig. 15 — (A) B_{11} *vs* Ns; and (B) B_{11} *vs* Be

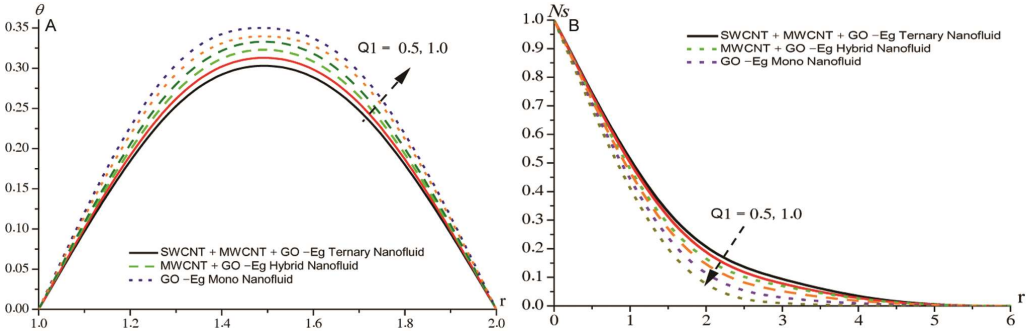

Fig. 16 — (A) Q_1 *vs* θ; and (B) Q_1 *vs* Ns

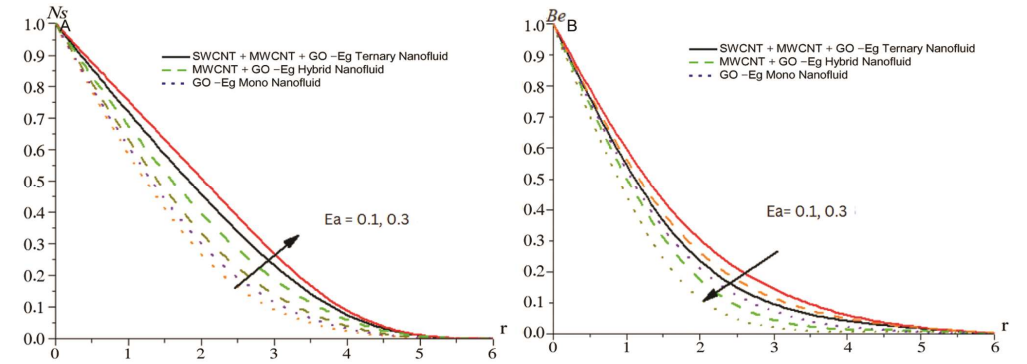

Fig. 17 — (A) Ea *vs* Ns; and (B) Ea *vs* Be

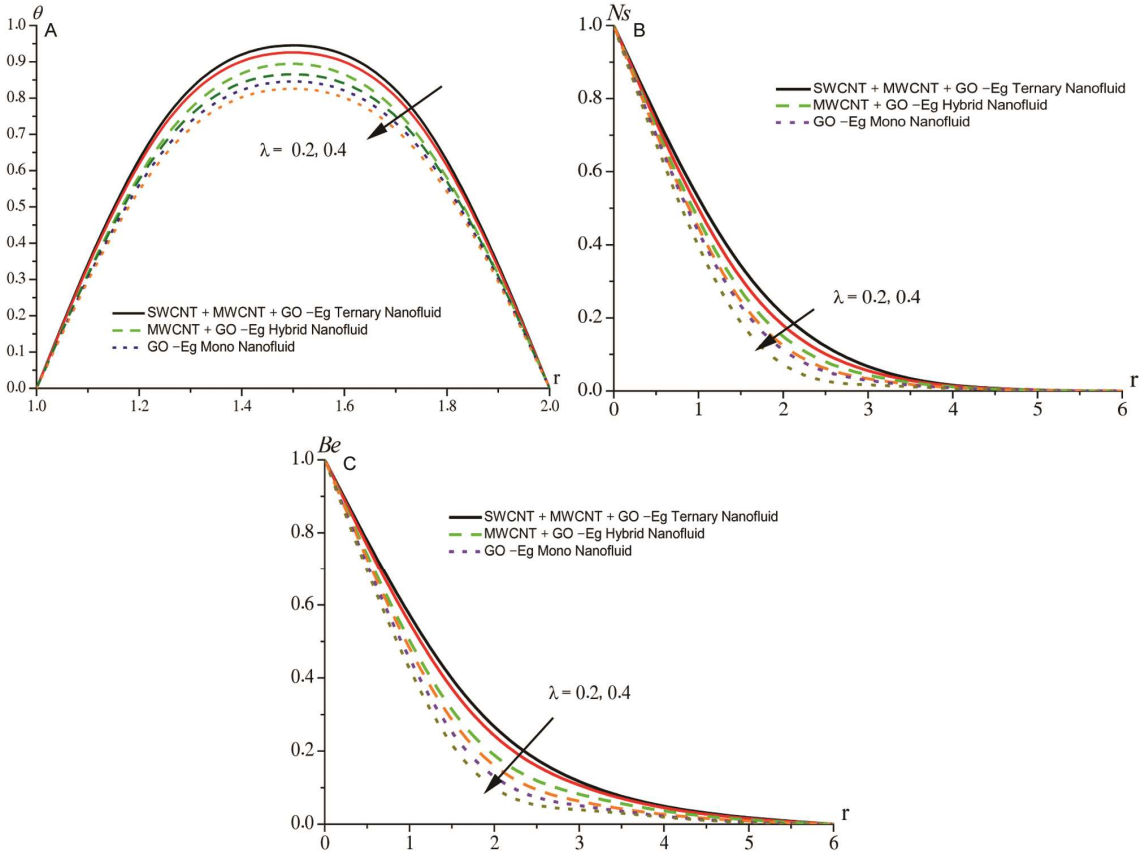

Fig. 18 — (A) λ *vs* θ; (B) λ *vs* Ns; and (C) λ *vs* Be

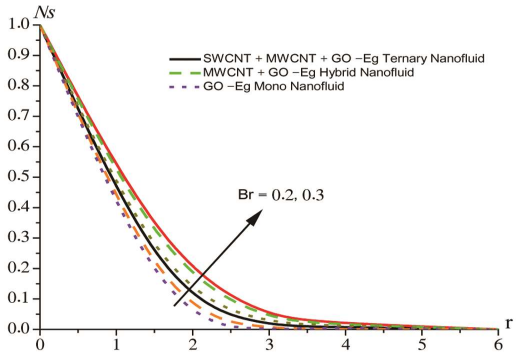

Fig. 19 — Br *vs* Ns

cylinder suggest that as factors like nanoparticle volume fraction, magnetic parameter, heat source parameters, and activation energy increase, heat transfer-driven entropy generation becomes the main factor, affecting the balance between heat transfer and fluid friction.

Tables 3 and 4 illustrates that shear stress at both cylinders (r=1 and r=2) increases with higher values of B, EcEc, B11, Sh, and activation energy E due to enhanced internal resistance to flow and increased heat generation, which elevates fluid friction. Conversely, an increase in the Grashof number, magnetic parameter (M), radiation absorption coefficient (Q1), and volume fraction (ϕ) reduces shear stress by enhancing heat diffusion, inhibiting fluid motion, or promoting buoyancy, thereby lowering frictional forces at the boundary. Ternary nanofluids, which minimize surface friction by reducing temperature gradients and viscous effects, exhibit lower shear stress than hybrid and mono-nanofluids due to their superior thermal conductivity. Additionally, the Nusselt number (Nu) at both the inner and outer cylinders increases with increasing G, Rd, A11, and ϕ as these factors enhance buoyancy-driven convection, thermal radiation, and thermal conductivity, thereby improving heat transfer. However, higher viscosity (B), Eckert number (Ec), and activation energy (E) reduce Nu due to greater fluid resistance, energy dissipation, and slower chemical reactions, which decrease heat transfer efficiency. Since ternary nanofluids possess higher thermal conductivity, enabling faster heat dissipation, they demonstrate superior heat transfer rates compared to hybrid and mono-nanofluids.

Table 3 — Skin friction (c_f), Nusselt number (Nu), Sherwood number with MWCNT + GO – Eg Ternary Nanofluid, MWCNT + GO – Eg, Hybrid Nanofluid and GO – Eg Mono Nanofluid at r = 1

Para-meters	SWCNT+MWCNT + GO – Eg Ternary Nanofluid			MWCNT + GO – Eg Hybrid Nanofluid			GO – Eg Mono Nanofluid		
	C_f	Nu	Sh	C_f	Nu	Sh	C_f	Nu	Sh
G	-0.693933	0.959313	1.65936	-0.694214	0.954955	1.65892	-0.694994	0.954665	1.65792
2	-0.680373	0.960756	1.66043	-0.680691	0.956395	1.66008	-0.685591	0.957595	1.65708
4									
M	-0.693933	0.959313	1.65936	-0.694214	0.954956	1.65892	-0.694994	0.954957	1.65772
0.5	-0.693323	0.959324	1.65943	-0.693594	0.954963	1.65899	-0.694059	0.954963	1.65889
1.0									
K	-0.693933	0.959313	1.65936	-0.694214	0.954953	1.65892	-0.694994	0.953957	1.65869
0.2	-0.693845	0.959606	1.70449	-0.694127	0.955244	1.70406	-0.689127	0.952994	1.70356
0.4									
B	-0.693933	0.959313	1.65936	-0.694214	0.954955	1.65892	-0.694214	-0.954054	1.65778
0.2	-0.771779	0.951682	1.65306	-0.772177	0.947278	1.65253	-0.785477	0.946678	1.65250
0.4									
Rd	-0.693933	0.959313	1.65936	-0.694214	0.954953	1.65892	-0.694994	-0.953894	1.65865
0.5	-0.693473	0.969429	1.70554	-0.693699	0.966133	1.70529	-0.694099	0.964563	1.69929
1.6									
5.0									
Ec	-0.693933	0.959313	1.65936	-0.694214	0.954935	1.65892	-0.694994	-0.953294	1.65675
0.05	-0.694433	0.944308	1.65787	-0.694722	0.939848	1.65729	-0.695012	0.932358	1.65699
0.10									
A_{11}	-0.693393	0.959313	1.65936	-0.694214	0.954955	1.65892	-0.694994	-0.949954	1.65892
0.1	-0.693747	0.962358	1.70476	-0.694034	0.958006	1.70436	-0.693893	0.953996	1.70436
0.3									
B_{11}	-0.693933	0.959313	1.65936	-0.694214	0.954955	1.65892	-0.694994	-0.948994	1.65675
0.5	-0.694417	0.947641	1.70311	-0.694722	0.942822	1.70251	-0.695032	-0.940022	1.70121
1.0									
ϕ	-0.693933	0.959313	1.65936	-0.694214	0.954955	1.65892	-0.694214	-0.930054	1.65678
0.05	-0.693653	0.963646	1.65975	-0.693950	0.958873	1.65931	-0.694070	-0.958876	1.65868
0.10									
Sc	-0.69392	0.959312	1.65935	-0.694213	0.954953	1.65891	-0.694212	-0.953886	1.65678
0.24	-0.694401	0.944600	1.70300	-0.694702	0.940171	1.70243	-0.694899	-0.938971	1.70200
0.66									
γ	-0.693931	0.959312	1.65934	-0.694212	0.954954	1.65891	-0.694321	-0.953792	1.65663
0.5	-0.693932	0.959780	1.73175	-0.694181	0.955419	1.73135	-0.694010	-0.954016	1.73008
1.0									
Sr	-0.693933	0.959313	1.65936	-0.694214	0.954955	1.65892	-0.694344	-0.937874	1.65562
0.5	-0.693914	0.959593	1.70327	-0.694198	0.955235	1.70263	-0.694200	-0.941223	1.70113
1.0									
Q1	-0.693933	0.959313	1.65936	-0.694214	0.954955	1.65892	-0.694394	-0.949994	1.65562
0.5	-0.694323	0.949135	1.70333	-0.694633	0.944352	1.65763	-0.694763	0.942152	1.65476
1.0									
Ea	-0.693933	0.959313	1.65936	-0.694214	0.954785	1.65892	-0.694304	-0.954599	1.65665
0.1	-0.693931	0.959225	1.64595	-0.694215	0.954862	1.64551	-0.694321	0.954342	1.64305
0.2									
δ	-0.694593	0.959313	1.65936	-0.694214	0.954954	1.65892	-0.694306	-0.944784	1.65447
0.1	-0.693929	0.959333	1.66292	-0.694212	0.954978	1.66248	-0.69429	0.950497	1.66048
0.2	-0.693929	0.959327	1.66197	-0.694213	0.954965	1.66154	-0.694301	0.954355	1.65674

Table 4 — Variations of C_f, Nu, and Sh at r = 2, with respsect to flow parameters

Parameter		C_f	Nu	Sh	C_f	Nu	Sh	C_f	Nu	Sh
G	2	0.590125	0.999837	0.585076	0.590340	1.00380	0.585090	0.590358	1.00445	0.585100
	4	0.584446	0.998700	0.584546	0.584675	1.00267	0.584543	0.584766	1.00290	0.584550
M	0.5	0.590124	0.999836	0.585077	0.590345	1.00380	0.585090	0.590459	1.00446	0.585100
	1.0	0.589594	0.999825	0.585037	0.589800	1.00378	0.585050	0.588602	1.00390	0.585063
K	0.2	0.590124	0.999836	0.585077	0.590346	1.00380	0.585096	0.590456	1.00441	0.585099
	0.4	0.590188	0.99962	0.572245	0.590408	1.00360	0.572260	0.590503	1.00365	0.572268
B	0.2	0.590120	0.999833	0.585079	0.590342	1.00379	0.585090	0.590459	1.00445	0.585100
	0.4	0.624344	1.006372	0.588367	0.624650	1.01039	0.588431	0.624763	1.01045	0.588447
Rd	0.5	0.590128	0.999835	0.585077	0.590348	1.00380	0.585092	0.590453	1.00441	0.585106
	1.0	0.589804	0.999825	0.571470	0.589974	1.00283	0.571480	0.590678	1.00100	0.571490
Ec	0.05	0.590127	0.999832	0.585078	0.590343	1.00380	0.585095	0.590100	1.00442	0.585100
	0.10	0.590595	1.016740	0.584302	0.590813	1.02086	0.584429	0.590937	1.02099	0.584430
A11	0.1	0.590125	0.999832	0.585077	0.590345	1.00380	0.585094	0.590473	1.00450	0.585100
	0.3	0.589962	0.997190	0.572171	0.590180	1.00112	0.572170	0.590110	1.00123	0.572180
B11	0.5	0.590125	0.999833	0.585075	0.590342	1.00380	0.585092	0.590402	1.00441	0.585100
	1.0	0.590510	1.005233	0.572550	0.590742	1.00940	0.572610	0.590722	1.00944	0.572610
ϕ	0.05	0.590124	0.999833	0.585075	0.590343	1.00380	0.585092	0.590100	1.00443	0.585100
	0.1	0.589911	0.995921	0.585083	0.590152	1.00063	0.585033	0.590131	1.00070	0.585040
	1.1	0.590112	0.999829	0.585077	0.590330	1.0040	0.585091	0.590407	1.00382	0.585093
	0.2	0.587320	1.030572	0.599090	0.587464	1.03363	0.599250	0.587557	1.03378	0.599258
Sc	0.24	0.590124	0.999836	0.585077	0.590345	1.00380	0.585092	0.590541	1.00388	0.585100
	0.66	0.590585	1.016583	0.571466	0.590806	1.02064	0.571585	0.590765	1.02072	0.571588
γ	0.5	0.590123	0.999833	0.585075	0.590345	1.00380	0.585091	0.590476	1.00443	0.585100
	1.0	0.590100	0.999532	0.564574	0.590317	1.00348	0.564588	0.590334	1.00350	0.564590
Sr	0.5	0.590124	0.999831	0.585077	0.590343	1.00379	0.585093	0.590354	1.00445	0.585108
	1.0	0.590113	0.999633	0.573163	0.590331	1.00360	0.573170	0.590342	1.00366	0.573176
Q1	0.5	0.590127	0.999835	0.585078	0.590349	1.00380	0.585092	0.590353	1.00446	0.585100
	1.0	0.5904222	1.003854	0.57250	0.590660	1.00813	0.585378	0.590678	1.00824	0.585380
Ea	0.1	0.590128	0.999833	0.585077	0.590345	1.00380	0.585092	0.590365	1.00448	0.585100
	0.2	0.590128	0.999899	0.589131	0.590343	1.00387	0.589119	0.590364	1.00400	0.589123
δ	0.1	0.590127	0.999833	0.585075	0.590345	1.00380	0.585092	0.590368	1.00449	0.585100
	0.2	0.590126	0.999820	0.584383	0.590344	1.00379	0.584400	0.590352	1.00389	0.584407
	0.4	0.590125	0.959326	1.661972	0.590342	0.95494	1.661533	0.590354	0.95496	1.661556

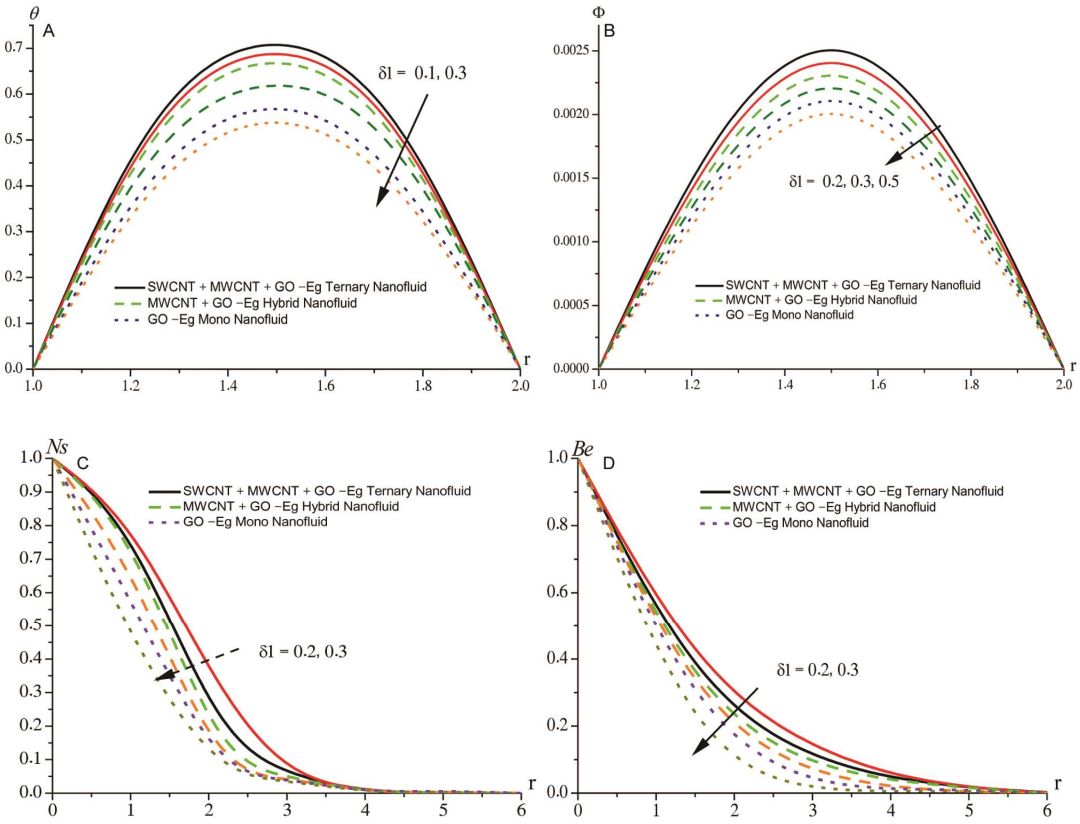

Fig. 20 — (A) δ1 *vs* θ; (B) δ1 *vs* Φ; (C) δ1 *vs* Ns; and (D) δ1 *vs* Be c2w`

The Sherwood number Sh indicates that the mass transfer rate increases at r=1 with increasing G, M, K, ϕ and heat source parameters A11 and B11 (Table 3). These parameters enhance convective flow, electromagnetic effects, and nanoparticle concentration, all of which promote mass transfer. On the other hand, as B, Rd, Ec, and Sr increase, mass transfer is suppressed by fluid resistance, energy dissipation, and thermal diffusion effects. For this reason, Sh decreases as these parameters increase. Because of their superior transport capabilities, ternary nanofluids usually exhibit higher mass transfer rates than hybrid or mono nanofluids.

Conclusion

The conclusions of this study highlight several key findings regarding the behavior and performance of ternary nanofluids in heat and mass transfer applications. It was observed that increasing parameters such as the Grashof number (G), magnetic parameter (M), heat source parameters (A_{11} and B_{11}), and volume fraction (ϕ) significantly enhances the Nusselt number (Nu) and Sherwood number (Sh), thereby improving the rates of heat and mass transfer. The results indicate that increasing the Grashof number (G) from 2 to 10 enhances the Nusselt number (Nu) by approximately 28%, while an increase in the magnetic parameter (M) from 0.5 to 2.0 leads to a reduction in velocity by nearly 35% due to the Lorentz force effect. Similarly, the heat source parameters (A_{11}, B_{11}) and volume fraction (ϕ) contribute significantly to improved heat and mass transfer rates, with a 20% increase in ϕ resulting in a 15% rise in Nu and an 18% boost in the Sherwood number (Sh). Conversely, fluid velocity was found to decrease with increasing ϕ, G, M, and A_{11} and B_{11}, while increasing with higher values of the Forchheimer parameter (Fr), activation energy (Ea), and mass transfer effects, demonstrating the complex interplay of these factors on flow dynamics.

Ternary nanofluids exhibited superior thermal and mass transfer properties compared to hybrid and mono nanofluids, resulting in higher fluid velocities. Additionally, entropy generation (Ns) was found to be highly sensitive to ϕ, M, and Ea, particularly near the inner cylinder, illustrating the influence of these parameters on thermodynamic irreversibilities. The analysis also revealed that activation energy

significantly impacts thermal conductivity, viscosity, and buoyancy-driven flow dynamics, ultimately influencing the overall thermal performance of nanofluids containing SWCNTs, MWCNTs, and Go/Eg.

These findings are particularly relevant for the design of advanced thermal management systems, such as high-performance electronics cooling, where efficient nanofluid cooling mechanisms are essential. While the current study provides valuable insights, future work could explore the effects of additional parameters such as chemical reactions, temperature-dependent properties, non-Darcy effects, and unsteady flow conditions to further enhance the understanding of heat and mass transfer processes in ternary nanofluids. By focusing on essential physical phenomena, this research offers a foundation for the application of ternary hybrid nanofluids in various engineering domains.

Nomenclature

	Description	SI Unit
T	*fluid temperature*	*Kelvin (K)*
u	*Axial velocity in porous media*	ms^{-1}
ρ	*fluid density*	kgm^{-3}
C_p	*specific heat at constant pressure*	$Jkg^{-1}K^{-1}$
$\nu = \frac{\mu}{\rho}$	*kinematic viscosity*	m^2s^{-1}
C	*fluid concentration*	Kg/m^3
μ	*Dynamic viscosity*	pas^{-1}
k	*Thermal conductivity*	$Wm^{-1}K^{-1}$
T_∞	*Ambient temperature*	K
C_w	*Fluid concentration at the plate*	Kg/m^3
D_m	*Mass diffusivity*	m^2/s
D_B	*Brownian diffusion coefficient*	m^2/s
K_T	*Mass diffusion coefficient*	m^2/s
β	*Thermal expansion coefficient*	K^{-1}
α	*Thermal diffusivity*	m^2/s
q_r	*Radiative heat flux vector*	W/m^2
Pr	*Prandtl number*	*Dimensionless*
g	*Acceleration due to gravity*	m/s^2
σ	*Reaction rate coefficient*	*1/s*
u_w	*Velocity of the Stretching sheet*	*m/s*

Conflict of interest

All authors declare no conflict of interest.

Acknowledgement

The author wishes to express sincere thanks to the honourable referees for the valuable comments and suggestions to improve the quality of the paper.

References

1 Choi SU & Eastman JA, Enhancing thermal conductivity of fluids with nanoparticles. *Argonne National Laboratory, DuPage County, IL, USA*; 1995.

2 Patil P, Shashikant A & Hiremath P, Influence of liquid hydrogen and nitrogen on MHD triple diffusive mixed convection nanoliquid flow in presence of surface roughness. *Int J Hydrogen Energy*, 43 (2018) 20101.

3 Hanif H & Shafie S, Impact of Al_2O_3 in electrically conducting mineral oil–based Maxwell nanofluid: Application to the petroleum industry. *Fractal Fract,* 6 (2022) 180.

4 Alami AH, Ramadan M, Tawalbeh M, Haridy S, Al Abdulla S, Aljaghoub H, Ayoub M, Alashkar A, Abdelkareem MA & Olabi AG, A critical insight on nanofluids for heat transfer enhancement. *Sci Rep*, 13 (2023) 15303.

5 Mahian O, Kianifar A, Kleinstreuer C, Moh'd AA, Pop I, Sahin AZ & Wongwises S, A review of entropy generation in nanofluid flow. *Int J Heat Mass Transfer*, 65 (2013) 514.

6 Kole M & Dey TK, Viscosity of alumina nanoparticles dispersed in car engine coolant. *Exp Therm Fluid Sci*, 34 (2010) 677.

7 Namburu PK, Kulkarni DP, Misra D & Das DK, Viscosity of copper oxide nanoparticles dispersed in ethylene glycol and water mixture. *Exp Therm Fluid Sci*, 32 (2007) 397.

8 Wang XQ & Mujumdar AS, Heat transfer characteristics of nanofluids: A review. *Int J Therm Sci*, 46 (2008) 1.

9 Singh N, Khullar V & Singh J, Corrosion behavior of copper and aluminum in nanofluid-based heat exchangers. *J Mater Sci,* 52 (2017) 1792.

10 Keblinski P, Eastman JA & Cahill DG, Mechanisms of heat flow in suspensions of nano-sized particles (nanofluids). *Int J Heat Mass Transfer,* 45 (2005) 855.

11 Said Z, Sajid MU, Ali HM & Saidur R, Recent advances on the application of nanofluids in oil recovery: Rheology, interfacial tension, and wettability. *J Mol Liq,* 307 (2020) 112972.

12 Sundar LS, Sharma KV, Naik MT & Singh MK, Investigation of thermal conductivity and viscosity of Fe_3O_4 nanofluid for heat transfer applications. *Int Commun Heat Mass Transfer,* 54 (2014) 66.

13 Alkasasbeh, HT & Mohamed MKA, MHD (SWCNTS + MWCNTS)/H_2O-based Williamson hybrid nanofluids flow past exponential shrinking sheet in porous medium. *Front Heat Mass Transfer,* 21 (2023) 265.

14 Srivastava N & Johari R, Numerical approach based study of MHD viscous and viscoelastic immiscible fluids flow through porous channel. *Indian J Pure Appl Phys,* 63 (2025) 51.

15 Shao Y, Nayak MK, Dogonchi AS, Chamkha AJ, Elmasry Y and Galal AM, Ternary hybrid nanofluid natural convection

within a porous prismatic enclosure with two movable hot baffles: An approach to effective cooling. *Case Stud Therm Eng,* 40 (2022) 102507.

16 Sahoo RR & Kumar V, Development of a new correlation to determine the viscosity of ternary hybrid nanofluid. *Int Commun Heat Mass Transfer*, 111 (2020) 104451.

17 Samantaray SS, Misra A, Shaw S, Azam M, Chamkha AJ & Nayak MK, Hydro-magneto-thermal aspects of ternary composite nanomaterial over arbitrarily inclined thin needle influenced by linear and nonlinear slips. *Int J Mod Phys B*, 38 (2024) 2450234.

18 Rashad AM, Khan WA, Nabwey HA & Elmeky H, Heat and mass transfer of Oldroyd-B and Jeffery-Williamson ternary-hybrid nanofluids over a stretching sheet in a porous medium. *J Porous Media,* 27 (2024).

19 Nield DA & Bejan A, Convection in porous media. *Springer International Publishing AG*, Berlin; 2017.

20 Gopi P, Effect of heat generating sources on hydromagnetic convective heat transfer flow of rotating SWCNT and MWCNT nanofluid in vertical channel with inconstant viscosity. *J Eng Comput Archit,* 14 (2024) 76.

21 Mondal P & Mahapatra T, MHD double–diffusive mixed convection and entropy generation of nanofluid in a trapezoidal cavity. *Int J Mech Sci,* 208 (2021) 106665.

22 Venkatesan G & Reddy AS, Insight into the dynamics of blood conveying alumina nanoparticles subject to Lorentz force, viscous dissipation, thermal radiation, Joule heating, and heat source. *Eur Phys J Spec Top*, 230 (2021) 1475.

23 Gholinia M, Hoseini ME & Gholinia S, A numerical investigation of free convection MHD flow of Walters-B nanofluid over an inclined stretching sheet under the impact of Joule heating. *Therm Sci Eng Prog*, 11 (2019) 272.

24 Jawali CU & Chamkha AJ, Combined effect of variable viscosity and thermal conductivity on free convection flow of a viscous fluid in a vertical channel. *Int J Numer Methods Heat Fluid Flow*, 26 (2015) 18.

25 Liu D, Song YZ, Sun SL, Yang S, Ahmed B & Muhammad T, Heat transfer performance and entropy generation analysis of Taylor–Couette flow with a helical slit wall. *Case Study Therm. Eng,* 53 (2024) 103852.

26 Kiran Kumar T, Srinivasa Rao P & Shamshuddin MD, Effect of thermal radiation on non-Darcy hydromagnetic convective heat and mass transfer flow of a water-SWCNT's and MWCNT's nanofluids in a cylindrical annulus with thermodiffusion and chemical reaction. *Int J Mod Phys B*, 38 (2024) 2450011.

27 Manjunatha S, Ammani Kuttan B, Jayanthi S, Chamkha A & Gireesha BJ, Heat transfer enhancement in the boundary layer flow of hybrid nanofluids due to variable viscosity and natural convection. *Heliyon,* 5 (2019) e01469.

28 Tiwari RK & Das MK, Heat transfer augmentation in a two-sided lid-driven differentially heated square cavity utilizing nanofluids. *Int J Heat Mass Transf,* 50 (2007) 2002.

29 Tao LN, "On Combined and Forced Convection in Channels." *ASME J Heat Transfer*, 82 (1960) 233.

30 Renuka, P, Ganga, B & Abdul Hakeem AK, Effect of Space and Temperature Dependent Internal Heat Generation/ Absorption on Casson Fluid Flow in the Presence of an Inclined Magnetic Field. *Malaya J Matematik*, 6 (2018) 428.

31 Usman M, Hamid M, Zubair T, Ul Haq R & Wang W, Cu-Al_2O_3/Water hybrid nanofluid through a permeable surface in the presence of nonlinear radiation and variable thermal conductivity *via* LSM. *Int J Heat Mass Transfer,* 126 (2018) 1347.

32 Kumar KT, Remidi S, Nagapavani M, Prasad KV, Karthik K, Kumar R & Kumar RN, A numerical study on the radiative heat transfer aspects of hybrid nanofluid flow past a deformable rotating cone. *Multiscale Multidiscip Model Exp Des*, 7 (2024) 5719.